RESEARCH ARTICLE

Dynamics of PIV seeding particles in turbulent premixed flames

F. Picano · F. Battista · G. Troiani ·
C. M. Casciola

Abstract Particle image velocimetry (PIV) estimates the fluid velocity field measuring the displacement of small dispersed particles between two successive instants separated by a small time interval. The accuracy of the measurements depends on the ability of the particles to accommodate their velocity to the fluid fluctuations. When the fluid is subjected to extreme accelerations, the small but finite inertia prevents the particles from following the fluid, originating a substantial relative velocity. This effect is shown to be crucial for applications of PIV to turbulent premixed combustion, particularly in the product region at locations just behind the instantaneous flame front. The issuing inaccuracy may easily spoil the estimate of certain statistical observables which are of crucial importance in the theory of turbulent premixed combustion. By exploiting the direct numerical simulation of a model air/methane flame, a suitable criterion for proper particle seeding is validated and compared with the corresponding experiments with a combined PIV/OH-LIF (laser-induced fluorescence) system. The proposed parameter, the *flamelet Stokes number*, depends on particle properties and thermochemical conditions of the flame and substantially restricts the particle dimensions required for a reliable estimate of the relevant flow statistics.

F. Picano · F. Battista · C. M. Casciola (✉)
Department of Meccanica e Aeronautica, Sapienza University,
via Eudossiana 18, 00184 Rome, Italy
e-mail: carlomassimo.casciola@uniroma1.it

G. Troiani
ENEA C.R. Casaccia, Via Anguillarese 301, 00123 Rome, Italy

1 Introduction

Many fields of engineering are characterized by reacting flows where particles with different inertia and dimensions are transported. Dispersed particles are found, e.g., in solid-propellant rockets where metal powder is used to enhance the specific impulse or in reciprocating engines where soot may form due to combustion.

Small particles are also used to probe the flow velocity by measuring their displacements, e.g. particle image velocimetry (PIV). In turbulent combustion, PIV is the leading technique to obtain the velocity field since other sensors hardly survive in chemically and thermodynamically harsh environments and present strong sensitivity to temperature variations (Steinberg et al. 2008; Boxx et al. 2010; Troiani et al. 2009).

In the experimental study of reacting flows, PIV combines non-intrusiveness (common to the other optical techniques), spatial resolution and the capability to obtain information concerning interactions between turbulent fluctuations and combustion. The understanding of particle dynamics in turbulent reactive flows is necessary to select a seeding able to adequately tag the velocity field. As a matter of fact, real particles, unlike perfectly Lagrangian tracers, do not follow exactly the flow trajectories. Their inertia and finite dimensions induce different non-trivial phenomena such as small-scale clustering (Balkovsky et al. 2001; Bec et al. 2007; Gualtieri et al. 2009) or preferential accumulation (turbophoresis) (Reeks 1983; Righetti and Romano 2004; Rouson and Eaton 2001; Picano et al. 2009).

As well established, in turbulent flows the particle characteristic time-proportional to inertia-must be small when compared to the Kolmogorov time scale in order to correctly capture the finest details of the flow. In turbulent

combustion, the interaction between particles and thermal expansion adds, however, new phenomenologies. The limitations concerning the ability of particles to accurately follow the fluid become particularly severe for premixed flames, due to the abrupt heat release concentrated in a very thin region. To describe these implications, we limit here our discussion to premixed reacting flows in the *flamelet regime* (Peters 2000), which is the most common condition for turbulent premixed flames. According to this classification, the reacting flow can be locally considered as a two-fluid flow where fresh reactants and burnt gases are separated by a thin interface—the flame front—where chemical reactions take place. This interface locally behaves more or less as a thin laminar flame, although the inner structure and the local flame speed may differ slightly from the pure laminar case due to the straining induced by turbulent fluctuations (Poinsot et al. 1991). Since the reactions and the heat release occur in a thin region, the flame front induces abrupt fluid accelerations that particles cannot easily accommodate due to their small but finite inertia.

In the context of particle seeding suited for premixed combustion, several papers addressed the impact of thermophoresis and that of the non-homogeneity of refractive index, e.g. Sung et al. (1994), Bergthorson and Dimotakis (2006), Stella et al. (2001), Han and Mungal (2003). Thermophoresis amounts to a force that influences tiny particle motions within the reacting zone. Actually, the steep temperature gradient between reactants and products generates an unbalanced migration of particles driven by Brownian forces that results in a drift toward the cold gases. The other uncertainty source is associated with the gradient of the refractive coefficient generated by density fluctuations that causes image distortion and light sheet deformation, as explained in Bergthorson and Dimotakis (2006). Despite a number of interesting attempts, much less attention has been devoted, instead, to the potential errors induced by particle inertia in the velocity measurements of turbulent reactive flows.

The aim of the present paper is to address the effects of the finite inertia and to provide a criterion for the appropriate selection of the PIV seeding in turbulent premixed flames with special emphasis on the region near the instantaneous flame front. As it will be shown, dependently on the nature and thermodynamics conditions of the flame, the proposed criterion may easily lead to the selection of very small particles, if high accuracy is desired on all but the most simple observables. It often happens that such particles may be prone to strong thermophoretic effect (Sung et al. 1994). In such cases, optimal particle sizes should minimize the probing error formed by the combination of inertial and thermophoretic components. It is thus crucial to estimate beforehand the inertial inaccuracy in view of minimizing the global error, see Steinberg et al.

(2008), Boxx et al. (2010) for recent high accuracy measurements with sub-micrometric particles.

To evaluate inertial errors, the most straightforward approach would be the comparison between the actual fluid velocity and its estimate based on particle velocity. Since the fluid velocity is clearly experimentally unavailable, we are forced to exploit the direct numerical simulation (DNS) of a turbulent premixed Bunsen flame endowed with finite mass probing particles able to reproduce the main characteristics of actual PIV seedings.

The DNS data support a criterion based on a suitable *flamelet Stokes number* St_{fl}, defined in terms of the particle relaxation time and the characteristic time scale of the flame front, which, in the flamelet regime, is set by the expansion rate and is a thermochemical property of the mixture. Our conclusions are supported by PIV data acquired in conditions as close as possible to the numerical simulations. In addition, simple arguments provide a formula able to correct to leading order the estimated mean velocity, shown to work in a significant range of flamelet Stokes numbers.

Compared to mean flow quantities, much more stringent requirements are needed for the accurate reproduction of more complex statistical observables, such as turbulent fluxes, turbulence intensities, probability distribution function of velocity and velocity gradient within the flame front.

2 Theoretical considerations and implications for experiments

2.1 Particle dynamics across the flame front

In order to gain insight into particle motions and to discuss the issues arising from finite inertia effects, certain simplifying assumptions are necessary. As verified in most PIV applications, we consider small spherical particles at low concentration such that inter-particle collisions and force feedback on the fluid can be neglected.

For applications to turbulent combustion, the typical density ratio between particles and fluid ρ_p/ρ_f is order 10^3, e.g. alumina or glass particles in air. Under the above conditions, with particle density much larger than that of the fluid $\rho_p/\rho_f \gg 1$, the dynamical equation for dispersed particles reads (Maxey and Riley 1983; Stella et al. 2001):

$$m_p \frac{dv}{dt} = F_S + F_G + F_T, \tag{1}$$

where m_p and v are the particle mass and velocity, F_S, F_G and F_T are the Stokes, the gravitational and the thermophoretic force, respectively. Under common conditions, gravity does not affect the accuracy of PIV measurements. On the

contrary, thermophoretic motions, negligible for particles with diameter larger than 1 μm (Frank et al. 1999; Troiani et al. 2009), may become an issue for submicrometric seedings (Sung et al. 1994). In the following, we will focus on the effects of the sole particle inertia. In such conditions, Eq. 1 becomes:

$$\dot{v} = \frac{u - v}{\tau_p} \tag{2}$$

where u is the fluid velocity at the particle position, while

$$\tau_p = \frac{d_p^2 \rho_p}{18 \nu \rho_f} \tag{3}$$

is the particle relaxation time representing the lag in the response to fluid velocity fluctuations (here d_p is the particle diameter and ν the fluid kinematic viscosity). For vanishing τ_p, the particles behave as Lagrangian tracers.

In actual PIV implementations, the particle relaxation time must be small with respect to the smallest characteristic time scale of the flow, if extreme accuracy down to the instantaneous gradients is demanded. In fully turbulent flows, the width of the continuous spectrum of time scales is order of the square root of the Reynolds number, implying τ_p smaller than the Kolmogorov time scale of the flow τ_k. In the case of turbulent premixed combustion, the abrupt density variation across the instantaneous flame front produces strong fluid accelerations that result in even more restrictive limitations on the relaxation time. Actually, in this case, the time scale is set by the fast reactions occurring within the flame. In the flamelet regime, the proper time scale can be estimated from the laminar characteristics of the front, i.e.

$$\tau_{fl} = \frac{\delta_L}{\Delta u_{fl}}, \tag{4}$$

where δ_L is the thermal thickness of the laminar flame and Δu_{fl} the velocity jump across the front. The thermal thickness is defined as $\delta_L = (T_b - T_u)/|\nabla T|_{sup}$, where $|\nabla T|_{sup}$ is the maximum module of the temperature gradient within the flame front and T_b and T_u are the temperature of burned and unburned mixture, respectively. The thermal expansion, instead, drives the velocity jump $\Delta u_{fl} = S_L(T_b/T_u - 1)$, with S_L the laminar flame speed. Using the time scale of the flame τ_{fl}, the relevant Stokes number becomes

$$St_{fl} = \frac{\tau_p S_L(T_b/T_u - 1)}{\delta_L}. \tag{5}$$

The proper τ_p should be based on the density and viscosity calculated at a characteristic temperature of the process. In particular, as the temperature experiences a large variation across the front, a suitable choice is the average between hot and cold gases, $T_m = (T_b + T_u)/2$. Since

usually $\tau_{fl} < \tau_k$, such flamelet Stokes number controls the ability of the particles to reproduce the velocity statistics of a premixed turbulent flame.

Before presenting our data, it is worthwhile discussing an a priori estimate of the difference between particle and fluid velocity in the limit of small τ_p. In this limit, the acceleration of particle and fluid closely match, $du/dt \simeq dv/dt$, see e.g. Bec et al. (2007), Goto and Vassilicos (2006). Hence, the Eulerian form of the Eq. 2 yields

$$u - v \simeq \tau_p \frac{Du}{Dt}. \tag{6}$$

In the reference frame of the flamelet, the normal acceleration is

$$\frac{Du_n}{Dt} \simeq u_n \frac{du_n}{dx}, \tag{7}$$

where x is the coordinate normal to the front and u_n the normal velocity. The estimate for the acceleration follows:

$$\frac{Du_n}{Dt} \simeq S_L \frac{\Delta u_{fl}}{\delta_L} = S_L \frac{S_L(T_b/T_u - 1)}{\delta_L}. \tag{8}$$

From relations (6) and (8) the order of magnitude of the difference between fluid and particle normal velocity in the reaction region is given by:

$$|u_n - v_n| \simeq S_L St_{fl}. \tag{9}$$

2.2 Accuracy enhancement for mean velocity

The accuracy in the measured average fluid velocity may be enhanced by exploiting Eq. (2), rewritten as,

$$u = v + \tau_p \frac{Dv}{Dt} \tag{10}$$

where $Dv/Dt = \partial v/\partial t + v \cdot \nabla v$ is the Eulerian expression of the particle acceleration field, see Appendix A for a detailed derivation. Hence, a more accurate estimate of the fluid velocity field can be obtained by taking into account the particle acceleration. In terms of mean fields, the ensemble average of the Eq. (10) leads to

$$U = V + \tau_p[V \cdot \nabla V + \langle v' \cdot \nabla v' \rangle], \tag{11}$$

an equation that can be used in principle in its complete form (here $U = \langle u \rangle$ and $V = \langle v \rangle$ are the fluid and particle mean velocity, respectively, with angular brackets denoting average and a prime indicating fluctuating quantities). In many cases, however, the fluctuations provide a minor contribution which can be safely neglected, see Sect. 4, yielding the simpler correction formula,

$$U \simeq V + \tau_p V \cdot \nabla V. \tag{12}$$

The equations discussed in the present subsection are in fact a first-order correction to the standard assumption

$U \simeq V$, which may result inappropriate when the Stokes number is not negligibly small.

3 Numerical analysis

3.1 Assumptions and methodology

The behavior of particles in a turbulent premixed reactive flow is addressed by means of an Eulerian DNS of a turbulent Bunsen flame coupled with a Lagrangian solver for particle evolution.

The algorithm discretizes the Low-Mach number formulation of the Navier–Stokes equations in cylindrical coordinates, which describe a low-Mach number flow with arbitrary density variations neglecting acoustic effects (Majda and Sethian 1985).

The spatial discretization is based on central second-order finite differences in conservative form on a staggered grid. The convective terms of scalars are discretized by a bounded central difference scheme designed to avoid spurious oscillations (Waterson and Deconinck 2007). Temporal evolution is performed by a low-storage third-order Runge–Kutta scheme.

Time evolving Dirichlet data (prescribed velocity) are enforced at the inflow to simulate a turbulent inlet. A cross-sectional plane extracted from a companion DNS of a turbulent pipe flow serves the purpose. Convective and traction-free conditions are adopted at the outflow and at the side boundary, respectively. More details on the code and tests for incompressible jet and pipe flows can be found in Picano and Casciola (2007), Picano et al. (2009).

Chemical kinetics is assumed in the form of a global Arrhenius irreversible reaction transforming premixed fresh mixture R into exhaust combustion products P. The simulation reproduces a premixed Bunsen flame with fully developed turbulent inflow and Reynolds number $Re_D = U_0 D / \nu_\infty = 6,000$, with U_0 the bulk velocity and $D = 2R$ the nozzle diameter.

The simulation reproduces a lean premixed methane/air Bunsen flame (equivalence ratio $\phi \sim 0.7$, temperature ratio $T_b/T_u = 5.3$). The specific heat capacity ratio is assumed constant, $\gamma = c_p/c_v = 1.33$, and the dynamic viscosity is proportional to the square root of temperature, $\mu \propto T^{1/2}$. The ratio of laminar flame speed to bulk velocity is $S_L/U_0 \simeq 0.05$, with a laminar flame thickness $\delta_L \simeq 0.019\,D$. The computational domain, $[\theta_{max} \times R_{max} \times Z_{max}] = [2\pi \times 6.2D \times 7D]$, is discretized by $N_\theta \times N_r \times N_z = 128 \times 201 \times 560$ grid points. The mesh is uniform up to $r = 0.6\,D$ with a grid spacing of $0.00625D$ that is successively stretched linearly up to the external boundary. The grid is designed to assure optimal accuracy in the region where the instantaneous flame turns out to be confined, with a typical grid size everywhere below three times the Kolmogorov scale.

A snapshot of axial fluid velocity and flame front position is reproduced in Fig. 1, top panel, to provide an overall view of the instantaneous configuration of the flame. The bottom panel displays the reactant concentration profile across the instantaneous front at three axial distances. From the symbols, corresponding to the actual positions of the related grid nodes, an impression on the spatial accuracy of the simulation can be obtained. The solid line is the concentration profile for the corresponding laminar, unstretched 1D flame. The comparison validates the flamelet regime for the present flame.

The DNS results are in good agreement with the experimental data for the same configuration and Reynolds number, Fig. 2, see Troiani et al. (2009), Troiani (2009) for a detailed description of experimental set-up and technique. In the figure, axial and radial mean velocities are represented by the colored iso-levels with left and right part of the images providing experimental and numerical data, respectively.

Velocity measurements are performed with a commercial PIV system based on a 532 nm 54 mJ Nd:YAG LASER and a camera equipped with a lens whose focal length is 60 mm. The f-stop ranges between 4 and 5.6 to
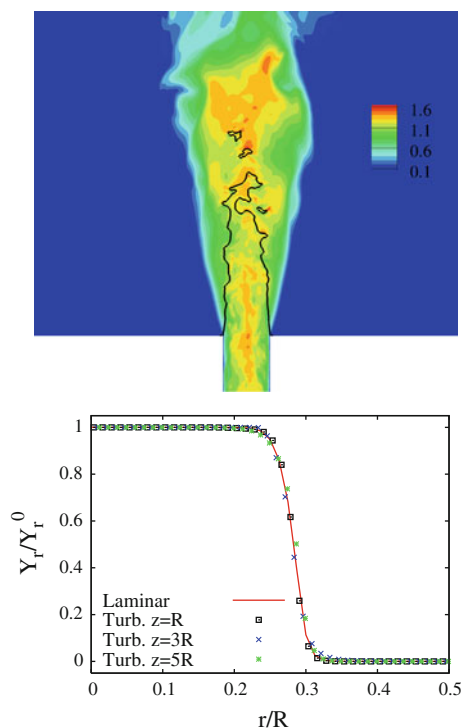

Fig. 1 *Top* instantaneous 2D cut of axial velocity (contours) and isolevel of reactants at $Y_r/Y_r^0 = 0.5$ (*solid line*). *Bottom* radial concentration profiles across the instantaneous flame front at three axial distances, $z/R = 1, 3, 5$ (*symbols*). The *continuous line* is the corresponding laminar 1D profile
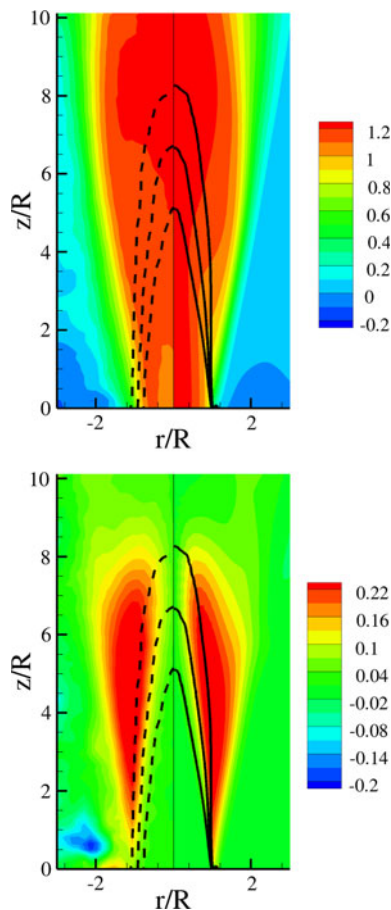
Fig. 2 Comparison of mean velocity field between present DNS and experimental data obtained at same Reynolds number $Re_D = 6,000$ and $S_L/U_0 = 0.05$. Experimental apparatus and techniques (PIV/OH-LIF) are described in Troiani (2009), Troiani et al. (2009). The mean velocity field normalized by bulk velocity U_0 is represented by flood-contours, while three iso-levels of mean progress variable, namely $C = 0.1$, $C = 0.5$ and $C = 0.9$, are displayed with *black lines*. In each *panel* the *left half-figure* represents experimental data, while the *right half-figure* the DNS ones. *Top panel* axial component; *bottom panel* radial component

accommodate the scattering signal of different sized particles avoiding saturation of the detector. The resolution of the CCD is $1,280 \times 1,024$ pixels with a field-of-view of 110.7 mm $\times$ 88.52 mm. The set-up guarantees a pulse-to-pulse delay of 70 µs with a maximum particle displacement less than one-quarter of the interrogation window (32 $\times$ 32 pixels with an overlap of 50% and spatial resolution of 2.7 mm).

The black dashed and solid lines in Fig. 2 are iso-levels of the mean progress variable $C = 1 - Y_R/Y_R^0$, where Y_R and Y_R^0 are the local and the inlet reactant concentrations, respectively. The mean progress variable ranges from 0 to 1 in the flame brush region moving from the fresh mixture toward the exhaust gases. In the experiments, left part of the figure, the mean progress variable is estimated in the limit of the Bray–Moss–Libby thin flame model

(Bray et al. 1995). The instantaneous progress variable is assumed to jump from 0 to 1 across the thin instantaneous flame front whose position is detected by the laser-induced fluorescence of the OH radical, OH-LIF (Troiani et al. 2009).

In more details, the flame front position is educed by recording the fluorescent emission of the *OH* radical stimulated by a 282 nm laser source obtained by pumping a tunable dye-laser with the Nd:YAG source. The *OH* emission is acquired by a $1,024 \times 1,024$ pixel ICCD equipped with a 78 mm Nikon quartz lens providing a resolution of 160 µm/pixel, with a 2×2 pixel binning. A narrow pass-band filter, 10 nm wide and centered at 310 nm, avoids spurious signals originated by other ultra-violet sources, more details in Troiani et al. (2009). A maximum gradient criterion has been adopted to extract the flame front position from the fluorescence signal. The estimated position of the instantaneous flame front is used to define the instantaneous field of progress variable c, taken to be one in the burned gases and zero in the fresh mixture (flamelet assumption). From the instantaneous configurations, the mean field $C = \langle c \rangle$ reported in the figure is evaluated by standard ensemble averaging.

In numerics, particles evolve by a Lagrangian tracking method that integrates Eq. (2) with the same Runge–Kutta scheme used for the fluid phase. Fluid velocities are interpolated at particles positions with second-order Lagrangian polynomials, see Picano et al. (2009) for details. Particles do not counteract on the flow (one-way coupling) and inter-particle collisions are neglected, as appropriate for the typical seeding used in PIV. Four particle populations are considered with flamelet Stokes numbers $St_{fl} = 0.022$, $St_{fl} = 0.54$, $St_{fl} = 2.16$, $St_{fl} = 8.65$, respectively, to mimic a laboratory Bunsen premixed flame ($U_0 = 4.5 \, \text{ms}^{-1}$ and $D = 20$ mm) seeded with alumina particles ($\rho_p \simeq 4,000 \, \text{Kg/m}^3$) with diameters $d_p = 1$ µm, $d_p = 5$ µm, $d_p = 10$ µm, $d_p = 20$ µm, respectively. The corresponding time constants τ_p of the particle populations ranges from ~ 9 µs for $d_p = 1$ µm to ~ 3.5 ms for $d_p = 20$ µm (the reference temperature is $T_m = (T_u + T_b)/2$), see e.g. Han and Mungal (2003), Willert et al. (2006), Tieszen et al. (2004), Shoshin et al. (2010). We remark that the particle relaxation time depends quadratically on the diameter and linearly on the density ratio.

Particles are introduced in the field at fixed rate with homogeneous distribution at the inlet section of the jet where their assigned velocity equals that of the local fluid. Overall, about 6 millions particles are used in the simulation.

Before collecting data for statistical analysis, the simulation was ran for $30D/U_0$ time units to guarantee the statistical steady state. One hundred complete fields, separated in time by $0.125D/U_0$, were gathered in the numerical data acquisition.
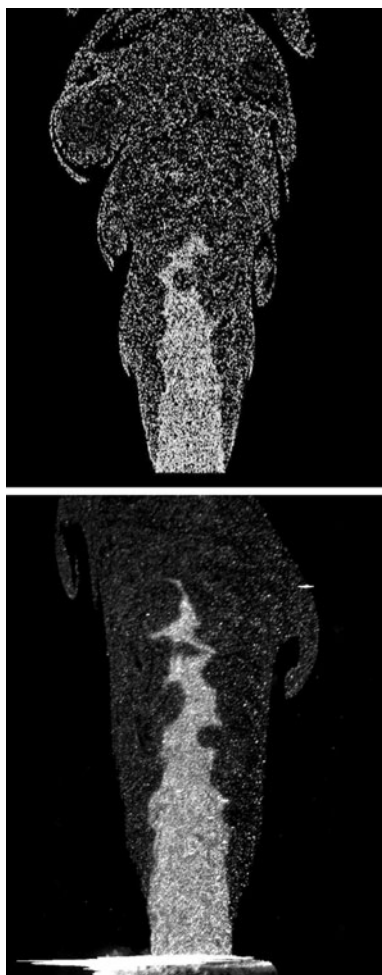
The particle configuration corresponding to the snapshot shown in the upper panel of Fig. 1 is shown in the upper panel of Fig. 3, where the effect of thermal expansion on particle density is apparent. A similar behavior is observed in the Mie-scattering experimental image reported in the bottom panel.

3.2 Results

3.2.1 Qualitative analysis

The effect of the variable-density flow on particles with different inertia is qualitatively shown in Fig. 4 where instantaneous configurations are presented. All particle populations exhibit in the exhaust gas region a reduced concentration due to the expansion experienced by the fluid across the flame front. This feature appears also in the experimental image of Fig. 3. Such abrupt change in
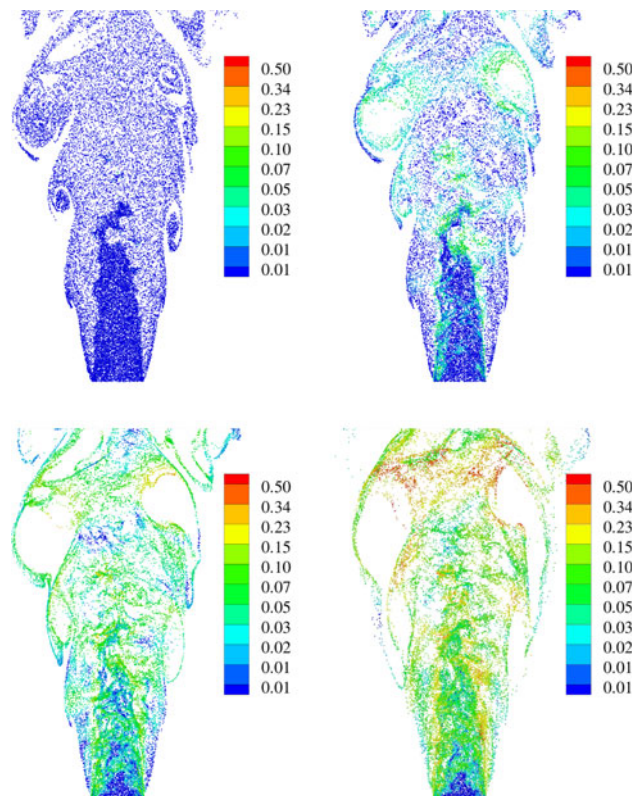

Fig. 4 Thin slice of width $D/40$ in the axial-radial plane of the instantaneous particle configuration for different Stokes times. *Top-left* $St_{fl} = 0.022$; *Top-right* $St_{fl} = 0.54$; *Bottom-left* $St_{fl} = 2.16$; *Bottom-right* $St_{fl} = 8.65$. *Colors* denote the norm of the difference between particle and fluid velocity: $|v - u|/U_0$

particle density across the front is a matter of technical concern for PIV applications, since, also for negligible particle inertia, it may induce a bias toward the reactant velocity whenever the interrogation window spans the flame.

At $St_{fl} = 0.022$ and 0.54, the normalized velocity difference $|v - u|/U_0$ shows that the fluid velocity is well reproduced by the particles, see Fig. 4. As the Stokes number increases, a progressively increasing mismatch occurs especially beyond the front, after the abrupt acceleration due to heat release. In particular, heaviest particles are not able to follow the basic flow features also when they are far away from the flame front.

Inertia also influences the spatial homogeneity of the instantaneous particle distribution. In all cases, particle clusters and intertwined voids are appreciated on a range of smaller and smaller scales as the Stokes number is reduced, see e.g. Gualtieri et al. (2009) where the effect is discussed in the context of a homogeneous shear flow. This phenomenon is particularly apparent in the burned gas region, especially for intermediate inertia particles where the typical void dimension is large enough to be clearly seen in the plot. The heaviest particles tend to be more

homogeneously distributed due to their inability to comply with the large-scale fluid motions.

Clustering may actually result in a source of noise in the cross-correlation analysis of particle positions, used in PIV to determine the velocity field. In this work, however, we address the accuracy of the velocity field estimate directly in terms of particle velocity. In addition, the spatial segregation of probing particles may induce systematic statistical bias associated with preferential sampling of fluid velocity events. We may anticipate that this aspect, briefly addressed in the following, has negligible impact on low-order statistical observables.

3.2.2 Mean velocity field

Figure 5 provides mean axial velocity profiles at two axial sections—$z = D$ and $z = 2D$—as a function of radial distance. Axial data are fairly well reproduced by the particles, at least when the Stokes number is not exceedingly large. The region of abrupt variation for the mean progress variable C–dashed line—is the so-called flame brush, see Sect. 3.1. Here, the heaviest particles cannot fully accommodate the steep velocity variations occurring across the
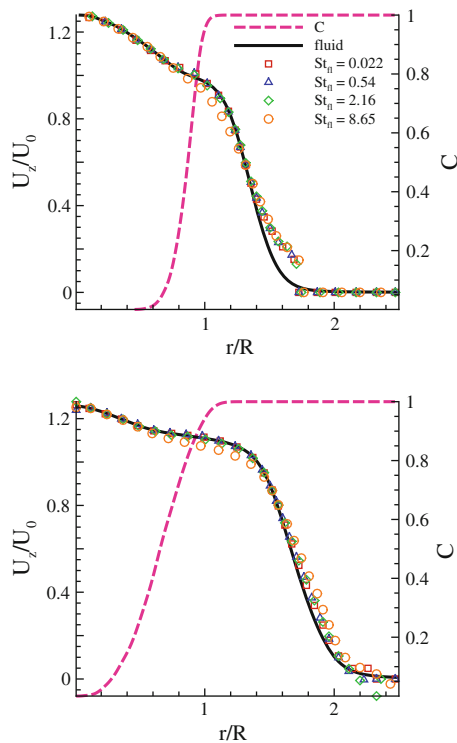
front resulting in a slightly biased estimate of mean axial velocity.

A more critical situation concerns the mean radial velocity displayed in Fig. 6. Since the normal to the flame front is mainly aligned with the radial direction, thermal expansion promotes a sudden radial acceleration of the fluid. In these conditions, appreciable errors emerge in the radial velocity estimation even for particles with flamelet Stokes number down to 2.16 (10 μm alumina particles in a lean methane/air flame). Still considering lean air/methane flames, the accuracy is greatly enhanced reducing the size of the alumina particles to five or one micron, as shown by the hollow squares and triangles in Fig. 6. As a generic feature, the shift in the peak position toward the burned gas systematically increases with the Stokes number. Shift and attenuation of the peak are clearly associated with the delayed response of the particles to the sudden acceleration through the front.

Since the surrounding environment is not seeded, a mismatch occurs between fluid and particle velocities in the outer part of the jet, where even the lightest particles manifest a substantial bias. This behavior is associated with the dynamics of the interface separating outer irrotational entrainment region and inner turbulent core, namely the highly intermittent viscous super-layer, see Corrsin and Kistler (1954), Sreenivasan and Meneveau (1986) for
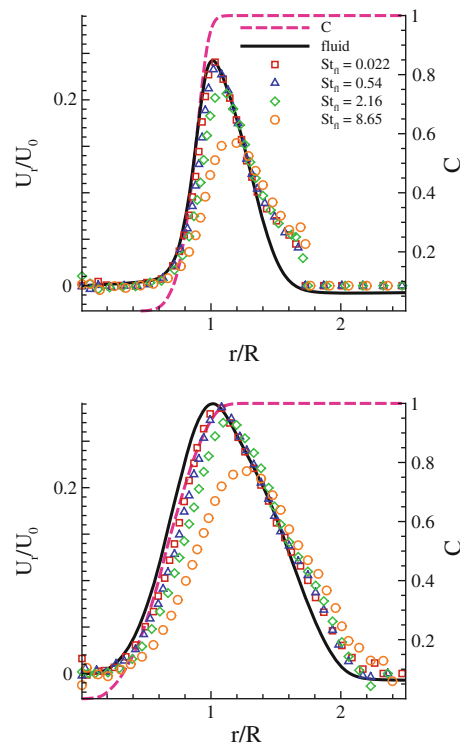

Fig. 5 Profiles of normalized Reynolds-averaged axial velocity U_z/U_0 as a function of r/R; *top panel*, $z/D = 1$; *bottom panel*, $z/D = 2$. *Black solid line* fluid velocity; *Symbols* particle velocity at different Stokes numbers; *dashed line* (*pink* in the electronic version): mean progress variable C

Fig. 6 Profiles of normalized Reynolds-averaged radial velocity U_r/U_0 as a function of r/R; *top panel*, $z/D = 1$; *bottom panel*, $z/D = 2$. Legend as in Fig. 5

incompressible cold jets. Here, the super-layer is external to the flame and separates the burned turbulent gases and the outer irrotational surrounding air. Quasi-Lagrangian (small) particles, injected in the turbulent region, hardly cross the super-layer. As a consequence, the statistics sampled by very light particles is biased by being systematically associated with the fluid in the turbulent state. In other words, quasi-Lagrangian particles always acquire the local fluid velocity, as shown in Fig. 7 by the uniform agreement of particle-conditioned fluid velocity and average particle velocity. Consistently, the persistent bias observed in Fig. 6 outside the flame brush should be ascribed to the non-uniform sampling of the outer part of the jet. On the contrary, the inner part, up to the entire flame brush region, is correctly sampled, as shown by the coincidence of the particle-conditioned with the unconditioned mean fluid velocity, Fig. 7. We conclude that the inertial errors in the mean radial velocity, Fig. 6, are not ascribed to sampling bias, as concerning the flame brush. Instead, the errors found in the outer part of the jet, outside the flame brush, are essentially associated to the non-uniform seeding of this highly intermittent region of the flow.

The magnitude of average fluid and particle velocity difference $\Delta U_r = \langle |u_r - v_r| \rangle$ is provided in Fig. 8, which is
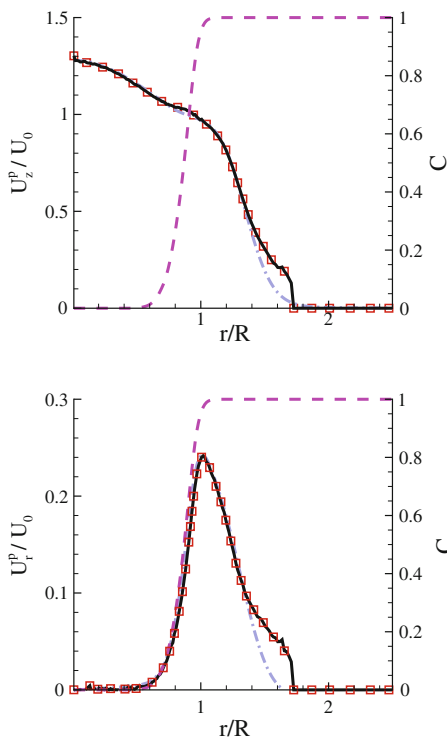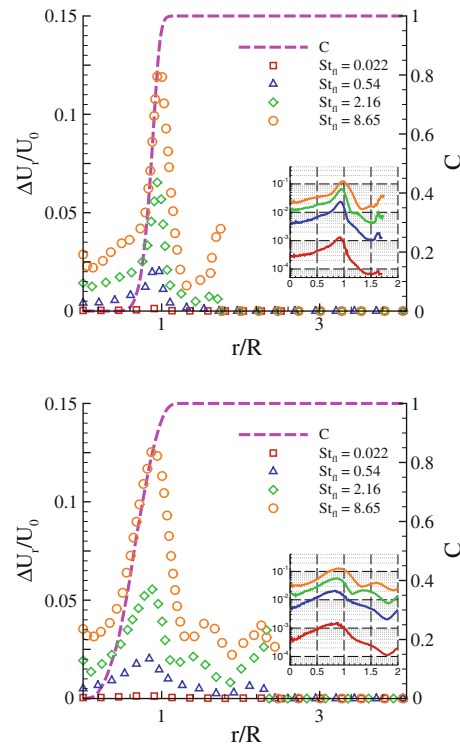

Fig. 8 Profiles of the averaged absolute values of the differences between particle and fluid radial velocity normalized by bulk velocity: $\langle |u_r - v_r| \rangle / U_0$; *top panel* at $z/D = 1$, *bottom* one at $z/D = 2$. In the *insets* the same statistics is provided in semi-log form. Legend as in Fig. 5

Table 1 Maximum error $\Delta U_r|_{max}/U_0$ at $z = 1D$ and $z = 2D$ and its estimate, Eq. (9)

St_{fl}	0.022	0.54	2.16	8.65
Estimated	1.1×10^{-3}	2.7×10^{-2}	0.11	0.43
$z = 1D$	1.3×10^{-3}	2.3×10^{-2}	0.07	0.12
$z = 2D$	1.5×10^{-3}	2×10^{-2}	0.06	0.12

focused on the radial, most critical component, mainly aligned with the normal to the flame front. The discrepancy increases monotonically with St_{fl}, and it is mainly concentrated in the flame brush. Table 1 reports the maximum error $\Delta U_r|_{max}$ for each population in comparison with the order of magnitude estimate (9), based on the small Stokes number approximation. The accuracy of the estimate is satisfactory up to $St_{fl} \leq 2.16$.

3.2.3 Second-order statistics

Axial $\langle u_z'^2 \rangle / U_0^2$ and radial $\langle u_r'^2 \rangle / U_0^2$ normal stresses are presented in Figs. 9 and 10, respectively. The overall behavior of the fluid is properly reproduced only by the smaller particles, $St_{fl} = 0.022$ and $St_{fl} = 0.54$, although an
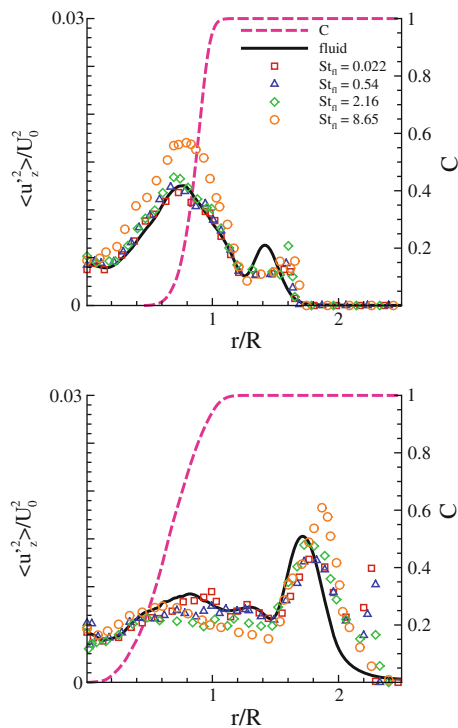

Fig. 7 $St_{fl} = 0.022$, $z/D = 1$. Mean fluid velocity conditioned to the presence of particles, *black solid lines*. Unconditioned mean fluid velocity, *gray dash-dotted lines*. Mean progress variable C, *dashed line* (*pink* in the electronic version). Average particle velocity, symbols. *Top panel* axial components; *bottom panel* radial components

Fig. 9 Profiles of normalized axial normal stresses $\langle u'^2_z \rangle / U_0^2$ as a function of r/R; *top panel*, $z/D = 1$; *bottom panel*, $z/D = 2$. Legend as in Fig. 5
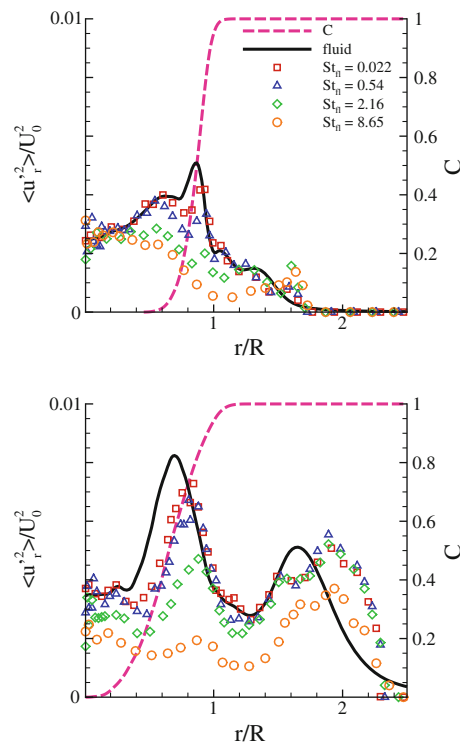
Fig. 10 Profiles of normalized radial normal stresses $\langle u'^2_r \rangle / U_0^2$ as a function of r/R; *top panel*, $z/D = 1$; *bottom panel*, $z/D = 2$. Legend as in Fig. 5

outward shift and an attenuation of the Reynolds stress peak is still apparent in the radial–radial component, Fig. 10. Particles with $St_{fl} = 2.16$, still acceptably capture the axial normal stress, but fail to reproduce the radial–radial component altogether. The heaviest particles are unfit to provide realistic measurement for the stresses. Clearly, the sampling bias observed in the outer part of the jet (large r/R) for the mean velocity (Fig. 7) is significant also for second-order statistics. These data unequivocally show that requirements for accurate reproduction of second-order statistics are more stringent than for mean velocity, requiring a flamelet Stokes number St_{fl} order of 0.1.

3.2.4 Front-conditioned statistics

As discussed in the previous sections, we found that the bias emerging in the flame brush is mainly due to the thermal expansion at the flame front. More detailed information can be gathered by looking at front-conditioned statistics. Their relevance can be appreciated by addressing the Bray–Moss–Libby (BML) formalism (Bray et al. 1995), where such statistical objects are used to determine the turbulent fluxes. In the BML context, the turbulent flux of the progress variable c is expressed as $\widetilde{u''_i c''} = \tilde{c}(1 - \tilde{c})(U^b_i - U^u_i)$, where $\widetilde{}$ and $''$ denote Favre averaging

and fluctuation, respectively. $U^b_i = \langle u_i | c = 1 \rangle$ and $U^u_i = \langle u_i | c = 0 \rangle$ are the mean velocity conditioned to products in the former case and to reactants in the latter. Clearly, turbulent fluxes are central objects in turbulent combustion and the BML model provides one of the few ways to extract them from combined PIV and OH-LIF experiments (Troiani et al. 2009; Frank et al. 1999).

Mean radial velocity conditioned to fresh gases U^u_r (numerically the nominal condition $c = 0$ is enforced by requiring $c \leq 0.05$), and conditioned to burned mixture U^b_r ($c \geq 0.95$), are displayed in Figs. 11 and 12, respectively. Analogously we can define the front-conditioned mean radial particle velocity V^b_r and V^u_r also reported in the same figures. The fluid unburned-conditioned statistics is reproduced by all particles with the exception of the most massive ones ($S_{fl} = 8.65$). The burned-conditioned velocity is instead much more demanding due to the sudden expansion across the thin flame front. Only the smaller particles, $St_{fl} = 0.022$ and $St_{fl} = 0.54$, provide high quality estimates. Particles with $St_{fl} = 2.16$ fail to reproduce the burned-conditioned radial velocity in the flame brush.

The biased response of the particles in the burned gas region has significant impact on the accuracy of the turbulent fluxes as estimated by the BML formalism, typically leading to an underestimation of the turbulent transport.
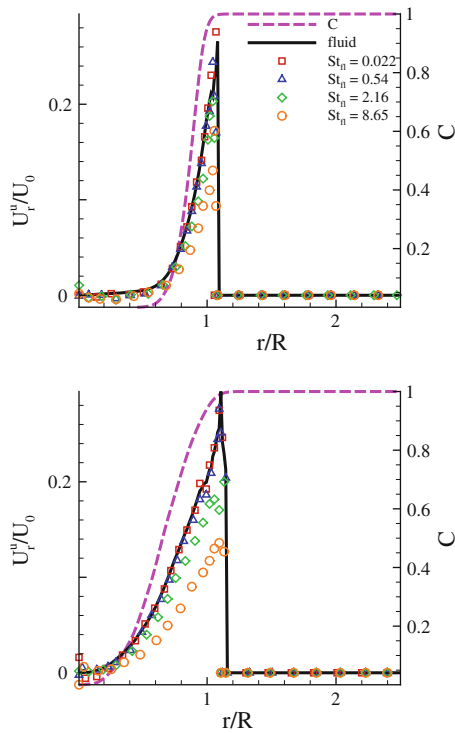
Fig. 11 Profiles of mean radial velocity conditioned to unburned mixture $U_r^u/U_0 - c \leq 0.05$. *Black line* fluid velocity; *Symbols* particles with different Stokes numbers; *dashed line* (*pink* in the electronic version): mean progress variable C. *Top panel*, $z/D = 1$; *bottom panel*, $z/D = 2$

Fig. 12 Profiles of mean radial velocity conditioned to the burned gases $U_r^b/U_0 - c \geq 0.95$. *Black line* fluid velocity; *Symbols* particles with different Stokes numbers; *dashed line* (*pink* in the electronic version): mean progress variable C. *Top panel*, $z/D = 1$; *bottom panel*, $z/D = 2$

Figure 13, top panel, provides the pdfs of particle and fluid radial velocities within the flame front at $z = D$. The inner region of the front is here determined by the interval [0.05, 0.95] for the instantaneous progress variable c. Formally, the probability distributions are actually conditional pdfs $p(u_r|c \in [0.05, 0.95])$. On average, the fluid velocity is directed away from the axis ($U_r > 0$), as expected. The process has a significant variance, comparable in magnitude with the mean value, and manifests a substantial intermittency, i.e. extreme events are much more frequent than expected on the basis of a Gaussian distribution with identical variance. It is immediately apparent that only the smallest particles are able to reproduce these rather subtle properties of the fluid pdf. The particles at $St_{fl} = 0.54$ are already unable the follow the right tail of the pdf, corresponding to events induced by the larger outwards accelerations. Increasing inertia, the modal value progressively decreases with a concurrent reduction of the process variance. At the same time, the pdf better and better approximates a Gaussian distribution.

Within the flame front, the radial–radial component of the fluid velocity gradient manifests a rather flat pdf, see bottom panel of Fig. 13. The figure shows that a significant deviation from the correct pdf is already observed for
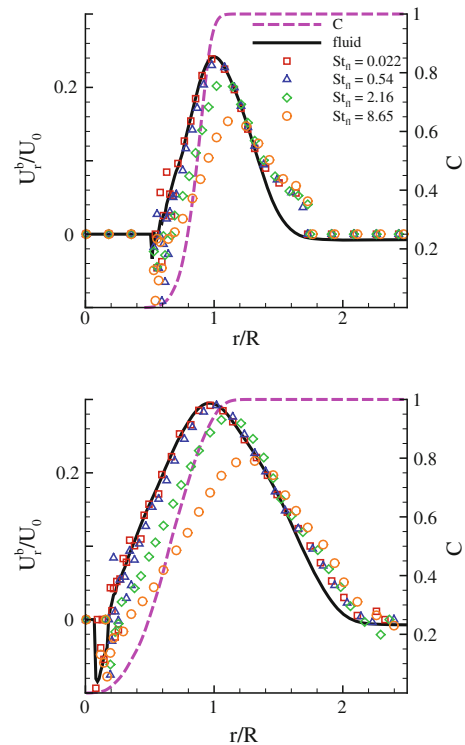
particles at $St_{fl} = 0.022$ with a significant bias already in the mean and modal value.

4 Improved estimate of the mean fluid velocity

Equation (12) supplies a first-order correction to the mean fluid velocity estimate.

Figure 14 provides a check of this formula by comparing the fluid mean radial velocity with both the mean particle velocity and the simplified form of the corrected expression

$$U_r \simeq V_r + \tau_p V_r \frac{\partial V_r}{\partial r}, \tag{13}$$

which retains only the dominating terms of Eq. (12).

As shown by Fig. 14, the corrected formula matches much more closely value and position of the fluid velocity peak for any particle population both at $z = D$ and $z = 2D$.

Figure 15 gives an overall impression on the accuracy enhancement achieved by applying the correction formula (13) to the raw data provided by the particles. The red curves (open symbols) in the top panel of the figure shows, for two axial locations, the error in the position of the radial
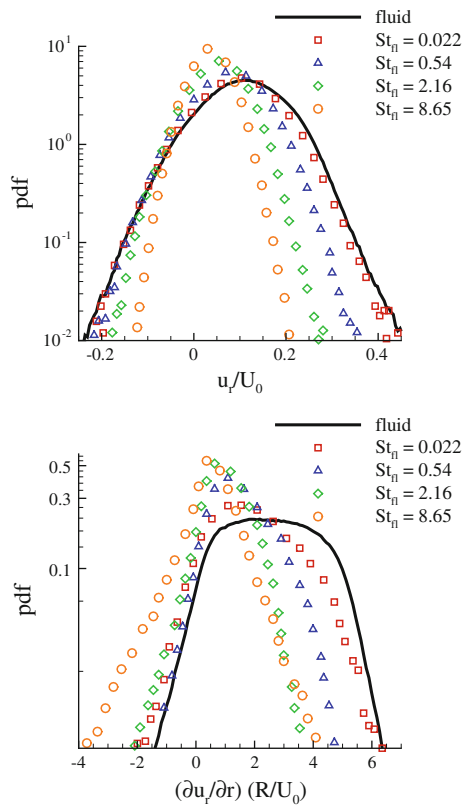
Fig. 13 Statistics within the instantaneous flame front ($0.05 \leq c \leq 0.95$) at $z = D$. *Top panel* pdf of particle and fluid radial velocity conditioned to $c \in [0.05, 0.95]$. *Bottom panel* pdf of radial derivative of radial particle and fluid velocity, same conditioning

Fig. 14 Radial profiles of normalized mean radial particle velocity (*open symbols*) and improvement based on Eq. (13) (*filled symbols*). *Black line* fluid velocity; *dashed line* (*pink* in the electronic version): mean progress variable C. *Top panel*, $z/D = 1$; *bottom panel*, $z/D = 2$

mean velocity peak as difference (in absolute value) between the estimate based on the particles and the actual position taken from the DNS simulation. The blue curves (closed symbols) provide the difference between the actual position of the peak (DNS simulation) and its estimate based on the correction formula (13). The bottom panel of Fig. 15 analogously concerns the error in the intensity of the peak both for raw particle and enhanced data. The ability of the correction formula in estimating the peak position is amazing. The accuracy in the peak intensity also increases, still requiring however sufficiently light particles to achieve a confidence interval below five percent.

5 Experimental validation

In order to analyze the effect of inertia on real particles, PIV measurements have been carried out in a Bunsen burner with three different particle populations varying the flamelet Stokes number. An air/methane stoichiometric mixture, seeded with the particles, has been injected into a Bunsen device at a Reynolds number of $Re_D = 8,000$ (nozzle diameter of 18 mm). At stoichiometric conditions,
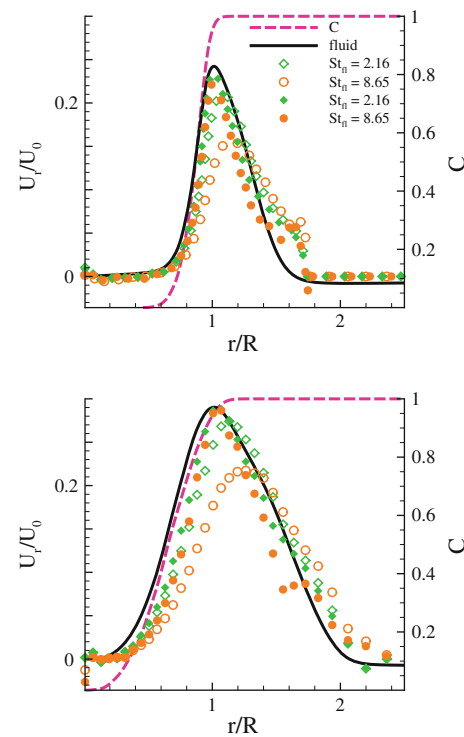
the characteristic time scale of the laminar front is of the order of $\tau_{fl} \simeq 0.16$ ms, as estimated by standard laminar flame computations (Kee et al. 1996). Two populations consist of alumina particles ($\rho_p \simeq 4,000$ Kg/m^3) with nominal diameter $d_p = 5$ μm and $d_p = 10$ μm, leading to $St_{fl} = 1.1$ and $St_{fl} = 4.4$, respectively. The third kind of particles were huge glass spheroids ($\rho_p \simeq 2,500$ Kg/m^3, $d_p = 50$ μm) with flamelet Stokes number $St_{fl} = 68.8$. Concerning the PIV system already described in Sect. 3.1, a thorough analysis of velocity measurement errors with alumina particles of 5 μm, here considered as the reference measurement, is reported in Troiani et al. (2009). To highlight the effect of the particle inertia, the same setup is used for all particles to keep the same level of optical accuracy (finite size of the interrogation windows).

The flame front induces an abrupt drop in the fluid density due to temperature increase. In fact, a steep thermal gradient does not necessarily imply the local existence of an actually burning front and conditioning to the presence of radical species is necessary, as possible by the combined PIV/OH-LIF technique already illustrated in Sect. 3.1. Nonetheless, in the present case, the thermo-chemical conditions and the jet-exit velocity of the flame have been selected to achieve a continuous flame front as expected on the basis of the standard Karlowitz criterion (Troiani 2009).
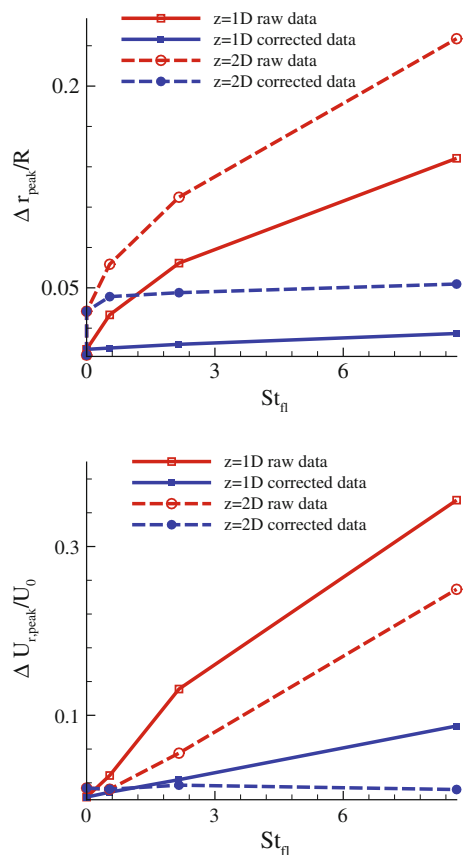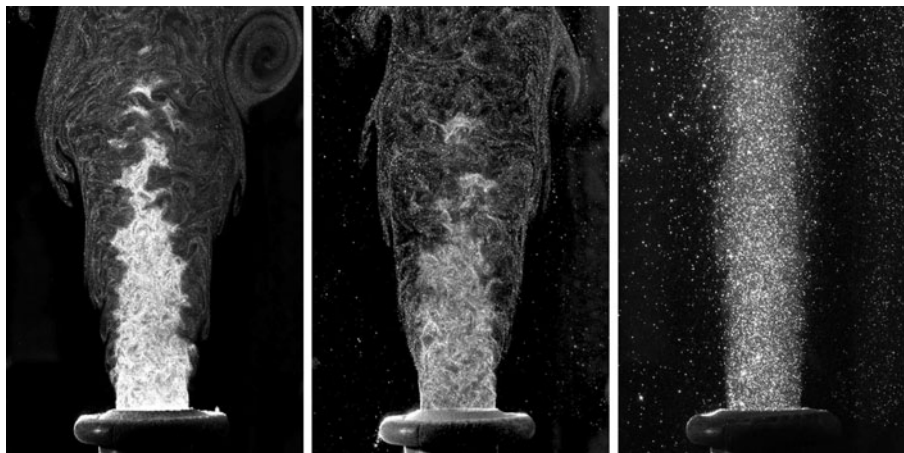
Fig. 15 *Top panel* normalized error in the radial peak position. *Bottom panel* normalized error in peak value. *Open symbols* (*red lines* in the electronic version), raw data; *Closed symbols* (*blue lines* in the electronic version), data corrected via Eq. (13)

density, as shown by Eq. (19) in the appendix, which implies $\nabla \cdot v = \nabla \cdot u + \mathcal{O}(\tau_p)$. This effect is apparent in Fig. 16, where moving from the right toward the left panel, i.e. reducing the particle relaxation time, the particle density contrast increases revealing finer details of the flame.

To quantitatively appreciate this effect, radial distributions of radial velocity have been examined, see Fig. 17 pertaining to $z/D = 2$. The thick dashed line (pink in the electronic version) provides the profile of the mean progress variable C. Open symbols refer to the mean radial particle velocity, showing for all three populations a velocity peak in the proximity of the average flame front. The particle inertia is reflected in the magnitude and position of the peak, which shifts toward the burned gases increasing St_{fl}. The comparison with the numerical results given in Fig. 14 confirms that the above-mentioned effect is to be ascribed to the finite mass of the particles. Dash-dotted lines with closed symbols represent data corrected with Eq. (13). The improvement in the results is apparent, compare top panel of Figs. 17 and 14. As quantified by the correction, the mean velocity as estimated by 5 μm particles is only slightly affected by inertia. A stronger bias is present in the other two cases. Nonetheless, the correction formula succeeds in restoring the position of the peak as can be clearly observed in the bottom panel of Fig. 17, still underestimating substantially the amplitudes. Clearly, the data concerning 50 μm particles are hardly representative of the flame behavior. Still Eq. 13 accurately estimates the peak position as can be seen in the bottom panel of Fig. 17.

Under these conditions, the thermal gradient, or equivalently the density gradient, can be accepted as a reasonable front-tracker.

Assuming the seeding particles able to follow the fluid motions almost exactly (vanishing τ_p), the change in fluid density induces a corresponding change in the particle

6 Final remarks

Beyond its fundamental interest, the dynamics of inertial particles in reacting flows is relevant for defining suitable criteria for PIV applications in turbulent premixed combustion. Actually, optical velocimetry commonly uses
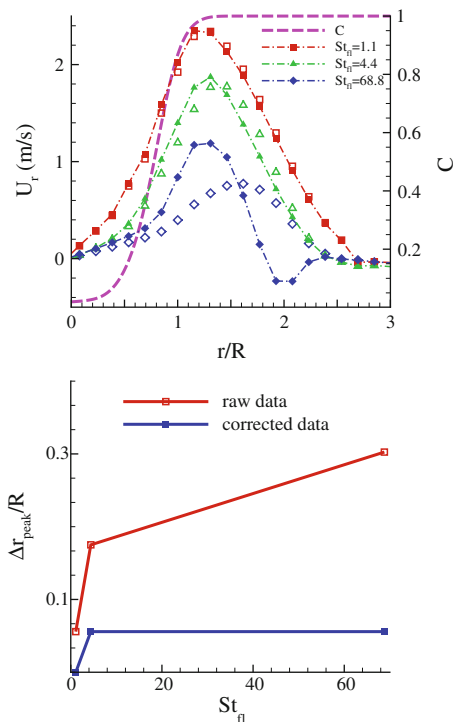
Fig. 16 Mie scattering of seeding particles for increasing inertia: *left*, alumina 5 μm; *center*, alumina 10 μm; *right*, glass 50 μm

Fig. 17 *Top panel* radial profiles of mean radial velocity (m/s) of particles measured by PIV for different particles (*open symbols*) and those given by the correcting formula (13) (*closed symbols*). *Dashed line (pink in the electronic version)*: mean progress variable C. Velocities have been measured at *z/D* = 2. *Bottom panel* normalized error in the radial peak position at *z/D* = 2. *Open symbols (red lines in the electronic version)*, raw data; *closed symbols (blue lines in the electronic version)*, corrected data

small particles to track the fluid velocity under the assumption of negligible fluid/particle relative velocity. In fact, the finite inertia of the particle always promotes a relative velocity difference, provided the characteristic time scale of the flow is sufficiently small. Though this is not usually an issue in non-reactive turbulent flows, in premixed combustion significant errors may be induced by the fast dynamics across the instantaneous flame front. In this context, the most stringent condition is found to concern the *flamelet Stokes number*, ratio of particle relaxation to flame front time scale. This parameter specifically controls the particle response to the fluid velocity fluctuations caused by combustion.

As soon as the flamelet Stokes number is smaller than unity, no significant errors occur on the estimated mean flow velocities. This condition is implicitly satisfied by most of the published papers using standard seeding particles on the order of 1 μm diameter for ordinary premixed flames (e.g. air/methane). The accuracy of the results obtained with slightly larger particles can be easily enhanced using the simple first-order correction formula discussed in Sect. 2.2.

However, turbulent combustion theory generally needs far more complex statistics. Typical examples are the turbulence intensities, the fluid velocity conditioned to the local state of the mixture, which enters, e.g., the expression of the turbulent fluxes according to the Bray–Moss–Libby formalism (Bray et al. 1995) and the probability distribution of fluid velocity and velocity gradients within the flame front. The present DNS results unequivocally show that the accurate estimate of these higher order statistics calls for a much lower limit on the admissible flamelet Stokes number, which may even be reduced of two orders of magnitude.

Given the definition of the relevant parameter, the flamelet Stokes number $St_{fl} = \rho_p d_p^2 / (18\,\mu)(S_L/\delta_L) (T_b/T_u - 1)$, chemical composition and thermochemical properties of the flame have a significant impact on the dimension of particles suited for accurate measurements, as direct consequence of the different flame speed, adiabatic flame temperature and front thickness.

As possible examples let us address a first case, where the mean velocity is the target of the measurement (design Stokes number $St_{fl} = 0.5$), and a second case targeting the much more demanding statistics within the flame front (design flamelet Stokes $St_{fl} = 0.01$). Considering a stoichiometric H_2/Air mixture at ambient conditions ($S_L \simeq 2.25$ m/s, $\delta_L \simeq 400\,\mu$m, $T_b/T_u \simeq 7.5$, $\mu \simeq 4 \times 10^{-5}$ kg/(ms) Law (2006)) the particle seeding diameter appropriate for mean velocity measurements is $d_p \simeq 1.5$ μm, which is reduced down to $d_p \simeq 0.2$ μm if accurate information within the front is desired. Increasing the pressure to 2 MPa the flame speed and thickness change to $S_L \simeq 1.25$ m/s, $\delta_L \simeq 10$ μm (Law 2006), yielding $d_p \simeq 0.3$ μm for the first and $d_p \simeq 0.05$ μm for the second case.

We remark that accuracy requirements based only on the inertial lag easily bring to select such small seeding particles that thermophoretic effect become substantial. In these conditions, the criterion here proposed could be used in principle to determine the largest particles compatible with the constraint on the inertial lag, at the same time minimizing the thermophoretic drift.

Appendix A: Eulerian formulation of particle velocity

In this appendix, we discuss a procedure to derive a continuum particle velocity field in terms of particle velocities in the limit of small τ_p. Starting from Eq. (2), we obtain the fluid velocity along the particle trajectory as the solution of $dx_p/dt = v_p$,

$$u[x_p(t), t] = v_p + \tau_p \dot{v}_p. \tag{14}$$

This allows to express the time derivative of the fluid velocity experienced by the particle as

$$\left.\frac{du}{dt}\right|_p = \frac{\partial u}{\partial t} + \dot{x}_p \cdot \nabla u = \dot{v}_p + \tau_p \ddot{v}_p. \tag{15}$$

The above expression yields

$$\frac{Du}{Dt} = (u - v_p) \cdot \nabla u + \dot{v}_p + \tau_p \ddot{v}_p, \tag{16}$$

which, rearranged as an expression for $\dot{v}_p$ to be inserted in (14), provides the fluid velocity as:

$$\begin{aligned} u &= v_p + \tau_p \left[\frac{Du}{Dt} + (v_p - u) \cdot \nabla u - \tau_p \ddot{v}_p \right] \\ &= v_p + \tau_p \frac{Du}{Dt} + \tau_p^2 (\dot{v}_p \cdot \nabla u - \ddot{v}_p). \end{aligned} \tag{17}$$

It follows

$$v_p = u - \tau_p \frac{Du}{Dt} + O(\tau_p^2). \tag{18}$$

Since both fluid velocity and acceleration are Eulerian fields, Eq. (18) defines an equivalent Eulerian particle velocity field by neglecting corrections of order τ_p^2,

$$v(x,t) = u(x,t) - \tau_p \frac{Du}{Dt}(x,t). \tag{19}$$

In this approximation, the particle velocities are treated as a single valued field. In its use one should be aware of the possible existence of caustics corresponding to a multi-valued particle velocity at the same position (Bec et al. 2005).

References

Balkovsky R, Falkovich G, Fouxon A (2001) Intermittent distribution of inertial particles in turbulent flows. Phys Rev Lett 86:2790

Bec J, Celani A, Cencini M, Musacchio S (2005) Clustering and collisions of heavy particles in random smooth flows. Phys Fluids, 17:073301

Bec J, Biferale L, Cencini M, Lanotte A, Musacchio S, Toschi F (2007) Heavy particle concentration in turbulence at dissipative and inertial scales. Phys Rev Lett 98(8):084502

Bergthorson JM, Dimotakis PE (2006) Particle velocimetry in high-gradient/high-curvature flows. Exp Fluids 41:255–263

Boxx I, Stöhr M, Carter C, Meier W (2010) Temporally resolved planar measurements of transient phenomena in a partially premixed swirl flame in a gas turbine model combustor. Combust Flame in press. doi:10.1016/j.combustflame.2009.12.015

Bray KNC, Libby PA, Moss JB (1995) Unified modeling approach for premixed turbulent combustion–part i: general formulation. Combust Flame 61(1):87–102

Corrsin S, Kistler AL (1954) Technical Report 3133, NACA

Frank JH, Kalt PAM, Bilger RW (1999) Measurements of conditional velocities in turbulent premixed flames by simultaneous oh plif and piv. Combust Flame 116:220–232

Goto S, Vassilicos JC (2006) Self-similar clustering of inertial particles and zero-acceleration points in fully developed two-dimensional turbulence. Phys Fluids 18(11):115103

Gualtieri P, Picano F, Casciola CM (2009) Anisotropic clustering of inertial particles in homogeneous shear flow. J Fluid Mech 629:25

Han D, Mungal MG (2003) Simultaneous measurements of velocity and ch distributions. Part 1: jet flames in co-flow. Combust Flame 132:565–590

Kee RJ, Rupley FM, Meeks E, Miller JA (1996) CHEMKIN-III: a FORTRAN chemical kinetics package for the analysis of gas-phase chemical and plasma kinetics. Sandia national laboratories report SAND96-8216

Law CK (2006) Combustion physics. Cambridge University Press, Cambridge

Majda A, Sethian J (1985) The derivation and numerical solution of equation for zero mach number combustion. Combust Sci Tech 42:185

Maxey MR, Riley JJ (1983) Equation of motion for a small rigid sphere in a nonuniform flow. Phys Fluids 26(4):883

Peters N (2000) Turbulent combustion. Cambridge University Press, Cambridge

Picano F, Casciola CM (2007) Small-scale isotropy and universality of axisymmetric jets. Phys Fluids 19(11):118106

Picano F, Sardina G, Casciola CM (2009) Spatial development of particle-laden turbulent pipe flow. Phys Fluids 21(9):093305

Poinsot T, Veynante D, Candel S (1991) Quenching processes and premixed turbulent combustion diagrams. J Fluid Mech 228:561–606

Reeks MW (1983) The transport of discrete particles in inhomogeneous turbulence. J Aerosol Sci 14(6):729–739

Righetti M, Romano GP (2004) Particle–fluid interactions in a plane near-wall turbulent flow. J Fluid Mech 505:93–121

Rouson DWI, Eaton JK (2001) On the preferential concentration of solid particles in turbulent channel flow. J Fluid Mech 428:149

Shoshin Y, Gorecki G, Jarosinski J, Fodemski T (2010) Experimental study of limit lean methane/air flame in a standard flammability tube using particle image velocimetry method. Combust Flame 157(5):884–892

Sreenivasan KR, Meneveau C (1986) The fractal facets of turbulence. J Fluid Mech 173:357

Steinberg AM, Driscoll JF, Ceccio SL (2008) Measurements of turbulent premixed flame dynamics using cinema stereoscopic PIV. Exp Fluids 44(6):985–999

Stella A, Guj G, Kompenhans J, Raffel M, Richard H (2001) Application of particle image velocimetry to combusting flows: design considerations and uncertainty assessment. Exp Fluids 30:167–180

Sung CJ, Law CK, Axelbaum RL (1994) Thermophoretic effects on seeding particles in ldv measurements of flames. Combust Sci Tech 99:119–132

Tieszen SR, O'Hern TJ, Weckman EJ, Schefer RW (2004) Experimental study of the effect of fuel mass flux on a 1-m-diameter methane fire and comparison with a hydrogen fire. Combust Flame 139(1–2):126–141

Troiani G (2009) Effect of velocity inflow conditions on the stability of a ch4/air jet-flame. Combust Flame 156(2):539–542

Troiani G, Marrocco M, Giammartini S, Casciola CM (2009) Counter-gradient transport in the combustion of a premixed ch4/air annular jet by combined piv/oh-lif. Combust Flame 156(3):608–620

Waterson NP, Deconinck H (2007) Design principles for bounded higher-order convection schemes—a unified approach. J Comput Phys 224:182–207

Willert C, Hassa C, Stockhausen G, Jarius M, Voges M, Klinner J (2006) Combined piv and dgv applied to a pressurized gas turbine combustion facility. Meas Sci Technol 17:1670–1679